

Bulk Flow Motion Detection in the Local Universe with Pantheon+ Type Ia Supernovae

Maria Lopes¹, Armando Bernui¹, Camila Franco¹, and Felipe Avila¹

¹Observatório Nacional, Rua General José Cristino 77, São Cristóvão, 20921-400 Rio de Janeiro, RJ, Brasil
marialopes@on.br, bernui@on.br, camilafranco@on.br, fsavila2@gmail.com

(Received 19-Mar, 2024; Accepted 21-Mar, 2024; to appear in ApJ)

Abstract

The *bulk flow* in the Local Universe is a collective phenomenon due to the peculiar motions of matter structures, which, instead of moving in random directions, appears to follow an approximate dipole velocity flow. We apply a directional analysis to investigate, through the Hubble-Lemaître diagram, the angular dependence of the Hubble constant H_0 of a sample of Type Ia Supernovae from the Pantheon+ catalog in the Local Universe ($0.015 \leq z \leq 0.06$). We perform a directional analysis that reveals a statistically significant dipole variation of H_0 , at more than 99.9% confidence level, showing that matter structures follow a dipole bulk flow motion towards $(l, b) = (326.^{\circ}1 \pm 11.^{\circ}2, 27.^{\circ}8 \pm 11.^{\circ}2)$, close to the Shapley supercluster $(l_{\text{Shapley}}, b_{\text{Shapley}}) = (311.^{\circ}5, 32.^{\circ}3)$, with velocity $132.14 \pm 109.3 \text{ km s}^{-1}$ at the effective distance $102.83 \pm 10.2 \text{ Mpc}$. Interestingly, the antipodal direction of this dipole points close to the Dipole Repeller structure. Our analyses confirm that the gravitational dipole system Shapley-Dipole Repeller explains well the observed bulk flow velocity field in the Local Universe. Furthermore, we performed robustness tests that support our results. Additionally, our approach provides a measurement of the Hubble constant $H_0 = 70.39 \pm 1.4 \text{ km s}^{-1} \text{ Mpc}^{-1}$, at the effective distance 102.8 Mpc , $z \simeq 0.025$. Note that this value was obtained using the first order approximation of the Hubble law because our methodology is model-independent. If one assumes, for instance, cosmography at second order with the Λ CDM value $q_0 = -0.55$, which is a model-dependent hypothesis, then $H_0 = 72.6 \pm 1.5 \text{ km s}^{-1} \text{ Mpc}^{-1}$, but our results: bulk flow velocity, dipole direction and its statistical significance remain the same.

Keywords: Observational cosmology, Large-scale structure of the universe, Type Ia supernovae

1 Introduction

Our Local Universe is manifestly inhomogeneous, plenty of matter structures, like galaxies assembled in small groups or in galaxy clusters, and cosmic voids, with various underdense matter contents and sizes, around us [Rubin, 1951, de Vaucouleurs, 1953, Gregory and Thompson, 1978, de Lapparent et al., 1986, Tully and Fisher, 1987, Coles, 1996, Courtois et al., 2013, Tully et al., 2019, Avila et al., 2019, Franco et al., 2024]. Peculiar velocities of cosmic objects are the result of gravitational fields, which, in turn, are originated

by the surrounding matter distribution [Peebles, 1980, Kaiser, 1987]. Therefore, peculiar motions are one of the best tracers of matter density fluctuations in the universe.

Near the Local Group of galaxies, to which the Milky Way belongs, a large underdensity termed the *Dipole Repeller* (DR) was recently discovered [Hoffman et al., 2017]. Another prominent feature in our cosmic neighborhood is the *Shapley* supercluster [Raychaudhury, 1989, Scaramella et al., 1989], the largest cluster of galaxies of the Local Universe.

The system Shapley-DR acts, approximately,

as a *gravitational dipole system* producing a bulk flow motion of matter in the Local Universe [Hoffman et al., 2017]. In this scenario the DR acts as it were a repulsive body causing the evacuation of matter in its surroundings; on the other side, the Shapley supercluster acts as the dominant matter attractor, pulling matter structures from every side. One important motivation for studying this gravitational dipole system, and the features of the induced bulk flow, is due to the dynamical effects produced as large peculiar velocities in our nearby galaxies [Tully et al., 2019, Peterson et al., 2022], information needed to a better calibration of the standard candles for precise measurements of H_0 at low redshifts [Scolnic et al., 2018].

Measurements resulting from some earlier studies already suggested a large bulk flow [Rubin et al., 1976, Lynden-Bell et al., 1988]. More recently, reports in the literature (see, e.g., Hong et al. [2014], Kalbouneh et al. [2023], Mc Conville and Ó Colgáin [2023], Perivolaropoulos [2023]) have studied the magnitude and direction of this bulk flow velocity with diverse approaches and investigating various cosmic tracers, where these studies confirm the dipole nature of the bulk flow, but point out some differences in the velocity magnitude and/or direction [Turnbull et al., 2012, Scrimgeour et al., 2016, Qin et al., 2018, Avila et al., 2023, Watkins et al., 2023, Whitford et al., 2023].

In this work, we perform an accurate directional analysis of the Type Ia Supernovae (SNe Ia) data from Pantheon+ [Brout et al., 2022] to measure the bulk flow velocity, both in intensity and in direction. Our analyses differ from other studies in various aspects. First, our methodology follows previous studies looking for preferred directions on the sky using several cosmic tracers [Bernui et al., 2008, Marques et al., 2018, Kester et al., 2024]; second, to avoid systematics from different observables, we use only SNe Ia data from Pantheon+; this choice is a challenge due to the possibility of having few SNe in some directions of the sky; third, we measure H_0 and its uncertainty in a set of N directions, which covers the celestial sphere, performing a best fit procedure using the Pantheon+ catalog and its covariance matrix, without cosmological model assumptions; fourth, we perform consistency and robustness tests to support our analyses and results.

Our directional analysis confirms an approximate dipole behaviour of the Hubble constant, with a dipole direction close to the Shapley-DR direction. The statistical significance is obtained by comparison with a set of simulated maps, produced by randomizing the angular positions of the SNe sample in study, and repeating our directional analysis procedure. For consistency, our analyses scan the celestial sphere considering two angular resolutions, but our final results and conclusions are drawn from the best angular resolution, i.e., scanning the sky with $N = 192$ ($N_{\text{side}} = 4$) spherical caps.

The outline of this work is the following. In Section 2 we select the SNe data, subsample of the Pantheon+ SNe Ia catalog, for our directional analysis in the Local Universe. In Section 3 we describe in detail the directional analysis approach, including the measurements and uncertainties involved. In Section 4, we present the H_0 -maps, calculate their dipole component, and determine its statistical significance. In Section 5 we present our conclusions and final remarks. We leave for the Appendix our consistency and robustness tests that support our analyses.

2 Data: The Pantheon+ SNe Ia Catalog

The recently released catalog of SNe Ia *Pantheon+* [Brout et al., 2022], successor of the original *Pantheon* sample [Scolnic et al., 2018], compiles a larger number of SNe Ia events, with more precise data, and it includes events located in host galaxies whose distances were obtained using *Cepheids*. The Pantheon+ catalog contains 1701 type Ia SNe, with redshifts $0.001 \leq z \leq 2.26$, and their angular distribution is shown in the top panel of Figure 1 (in galactic coordinates, where the Milky Way is in the center of the figure).

In addition to encompassing several redshift reference frames, such as the cosmic microwave background (CMB), and Heliocentric, the Pantheon+ catalog offers a comprehensive collection of precise data. This includes the light curves, covariance matrix, distance modulus, bolometric magnitude, and their associated uncertainties [Scolnic et al., 2022]. In our analyses, we shall use the following information from SN Ia data: the sky angular position, the redshift, the distance modulus, the peculiar velocities, all with their re-

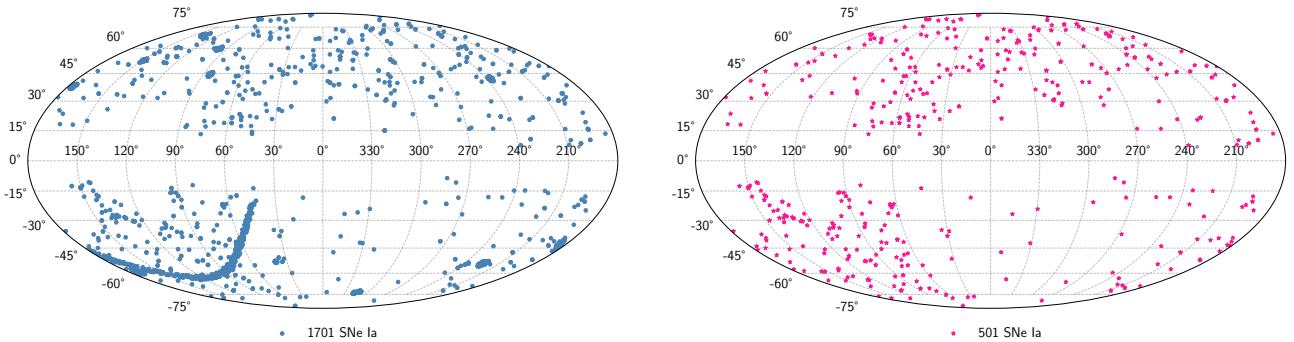


Figure 1: Distribution of SNe Ia on the celestial sphere with a Mollweide projection in galactic coordinates. **Left panel:** the Pantheon+ sample, showing 1701 SNe Ia. **Right panel:** the sample of 501 SNe Ia selected for our directional analysis, within the redshift interval $0.015 \leq z_{\text{CMB}} \leq 0.06$.

spective uncertainties except the last one, and the covariance matrix. Regarding the peculiar velocities' uncertainties, it is worth mentioning that they are undetermined (in the catalog appears the value 250 km s^{-1} for all the SNe listed there).

Our objective in this work is to detect the bulk flow motion in the Local Universe investigating the latest SNe Ia data from Pantheon+. The choice of the redshift interval for analyses was motivated by the following: (i) the gravitational dipole in analysis is limited by the region spatially close to the Shapley supercluster, where $z_{\text{Shapley}} \simeq 0.05$; for this, we consider data with $z_{\text{CMB}} \leq 0.06$; (ii) galaxies very close to us are not expected to follow the Hubble flow, as overdense and underdense regions in our neighborhood affect their motion, making it dominant over the Hubble expansion, then we adopt a conservative low-redshift limit $z_{\text{CMB}} \geq 0.015$ [Riess et al., 2016, Peterson et al., 2022]. In this case, our analyses are restricted to the Local Universe; therefore one can use the Hubble-Lemaître (HL) law to find H_0 [Visser, 2004]. Notice that, for consistency, in Appendix A we consider other four redshift intervals, close to $z_{\text{CMB}} \in [0.015, 0.06]$, where we apply our directional analysis to study the SNe samples contained in these intervals; as observed there, we basically obtain the same results.

According to these selection criteria, the sample chosen for analyses has 501 SNe Ia with redshifts $0.015 \leq z_{\text{CMB}} \leq 0.06$, i.e., measured in the CMB reference frame. The angular distribution of this sample is shown in galactic coordinates in the lower panel of Figure 1, and its redshift distribution is given in Figure 2.

3 Methodology

In this section, we present our methodology to perform the directional analysis of the set of 501 SNe Ia selected in the previous section from the Pantheon+ catalog. Our study consists in determining the value of H_0 in different sky directions. For this we define a set of N directions, chosen according to the HEALpix scheme, that uniformly scan the celestial sphere with spherical caps of angular radius γ centered at these N directions. Our directional analysis considers two angular resolutions to scan the celestial sphere: with $N = 48$ ($N_{\text{side}} = 2$) and $N = 192$ ($N_{\text{side}} = 4$) spherical caps. Then, we perform the best fit analysis in the HL diagram for those SNe Ia inside the i th spherical cap, centered at direction i , obtaining the best fit value $H_0^{b-f} \rightarrow H_0^i$ at the i th direction. We repeat this procedure for the N directions, obtaining the data set $\{H_0^i\}$, for $i = 1, 2, \dots, N$. The details of this analysis will be discussed in Section 3.2.1.

3.1 Finding H_0 with the Hubble-Lemaître Law

In the CMB reference frame, the measured velocity of any cosmic object is [Courteau and van den Bergh, 1999, Baumann, 2022]

$$\vec{v} = H_0 \vec{r} + \vec{v}_{pec}, \quad (1)$$

where peculiar motions contribute to deviate cosmic objects from the Hubble flow (i.e., the universe expansion). Considering the radial component of this equation, one obtains

$$c z_{\text{CMB}} = H_0 D + v_{pec}^r, \quad (2)$$

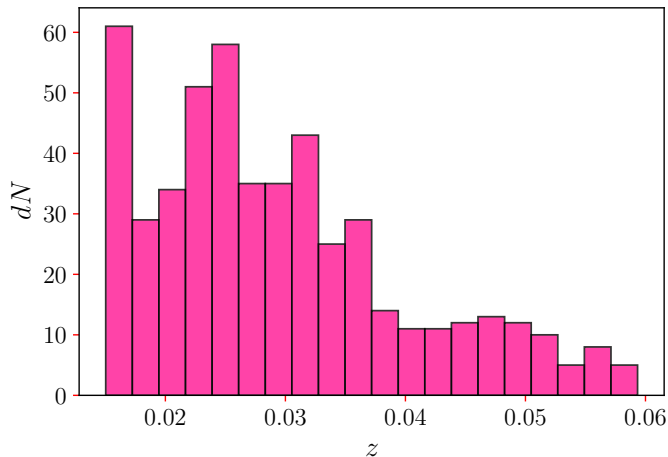


Figure 2: Frequency histogram of the 501 SNe Ia sample selected for our directional analysis, in different redshift intervals within the range $0.015 \leq z_{\text{CMB}} \leq 0.06$; the bin size is $\Delta z = 0.002$.

where D is the radial physical distance to the cosmic object, and v_{pec}^r is the radial projection of its peculiar velocity (to simplify the notation, from now on, we write: $v_{pec} = v_{pec}^r$).

The way we adopt to minimize the impact of the peculiar velocities is to choose for analysis SNe with $z_{\text{CMB}} \geq 0.015$, because in such a case, the peculiar velocities are a small fraction of the radial recession velocity. In fact, as observed in the plots shown in Figure 3 the peculiar velocities of our sample in analysis are, on average, lower than 5% of the recession velocity at redshifts $z_{\text{CMB}} \geq 0.015$. The impact of the SNe peculiar velocities will be considered later in our analyses, in Section 4.2.1.

3.1.1 Luminosity distance

To estimate the value of the Hubble constant, H_0 , through a best fit analysis, we use the SNe Ia luminosity distance and the redshift of each SN. In the Local Universe, luminosity distance is a good approximation for estimating proper distances to objects with small redshifts, $z < 0.2$ [Visser, 2004]. In effect, to perform the best fit for H_0 , we use the first-order expansion of the luminosity distance derived for the HL law, resulting from the series expansion for the physical distance $D(z) = D_L(z)$,

$$D_L(z_{\text{CMB}}) = \frac{c z_{\text{CMB}}}{H_0}, \quad (3)$$

where z_{CMB} is the SN redshift in the CMB frame.

To calculate the SNe Ia luminosity distances, we use the distance modulus μ , where the fidu-

cial magnitude was determined from SNe host distances [Brout et al., 2022]. The distance modulus is defined as the difference between the apparent magnitude m_B and the absolute magnitude M_B [Sparke and Gallagher, 2007]

$$\mu \equiv m_B - M_B = 5 \log_{10}(D_L/\text{Mpc}) + 25, \quad (4)$$

where D_L is given in Mpc. Then, we calculate the luminosity distance as

$$D_L = 10^{\frac{\mu-25}{5}}. \quad (5)$$

3.1.2 Uncertainties associated to D_L and δH_0

To determine the 1σ uncertainty of a function X that depends on two or more variables u, v, \dots , $X = f(u, v, \dots)$, we calculate it by quadrature

$$\sigma_x = \sqrt{\left(\frac{\partial X}{\partial u}\right)^2 (\sigma_u)^2 + \left(\frac{\partial X}{\partial v}\right)^2 (\sigma_v)^2 + \dots}, \quad (6)$$

where the terms $\frac{\partial X}{\partial u}$, $\frac{\partial X}{\partial v}$, \dots , are the partial derivatives of X with respect to u, v, \dots , and $\sigma_u, \sigma_v, \dots$, are the uncertainties associated with the measured quantities u, v, \dots , respectively. According to this, the errors associated to measurements of the luminosity distance, D_L , are

$$\sigma_{D_L} = \frac{1}{5} \ln(10) D_L \sigma_\mu, \quad (7)$$

where σ_μ is directly obtained from the Pantheon+ catalog. To estimate the error of H_0 we take into account the uncertainties from the best fit procedure, which in turn uses the covariance matrix

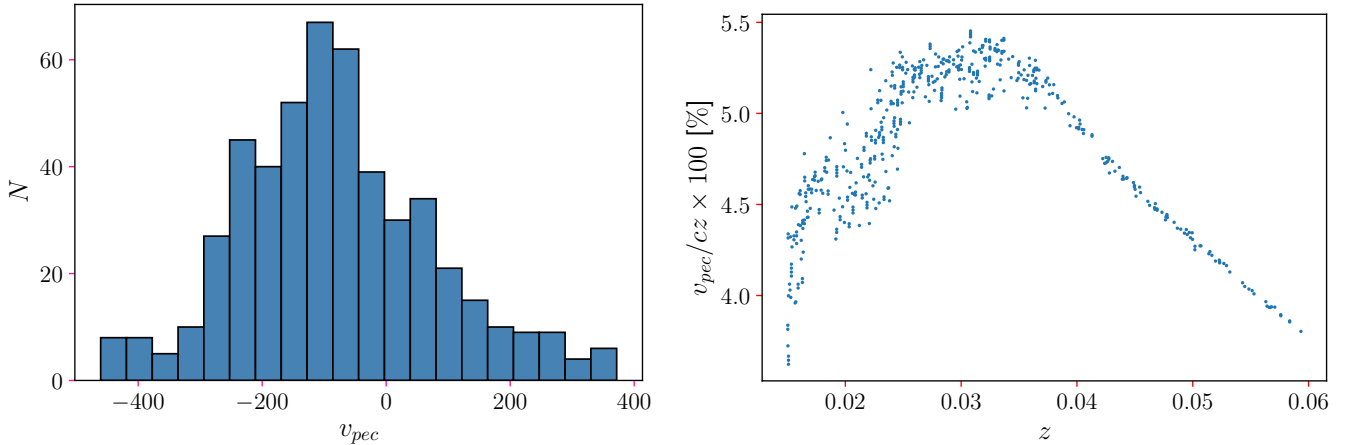


Figure 3: **Left panel:** peculiar velocities histogram of the 501 SNe Ia selected for our bulk flow analyses; this histogram shows that mean -81.87 , median -97.44 , and standard deviation 157.90 , all in units of km s^{-1} . **Right panel:** fraction, in percentage, of the peculiar velocities with respect to the recession velocity for the sample in analysis.

of the Pantheon+ sample, and also consider the statistical error due to the number of SNe Ia in each spherical cap. Therefore, the total error in the measurement of H_0 is

$$\sigma_{H_0} = \sqrt{\sigma_{b-f}^2 + \sigma_{st}^2 + \sigma_{dp}^2}, \quad (8)$$

where σ_{b-f} is the uncertainty in the best fit, and σ_{st} corresponds to the statistical error calculated as

$$\sigma_{st}^i = \frac{1}{\sqrt{n_i}}, \quad (9)$$

where n_i is the number of SNe Ia observed in the spherical cap i , and σ_{dp} corresponds to the uncertainty due to the dipole nature of the H_0 -map (see Section 4.1) uncertainty to be calculated using a Monte Carlo simulation in Appendix B.

3.2 The SNe H_0 -maps

To investigate in what direction our sample of 501 SNe Ia, with redshifts $0.015 \leq z \leq 0.06$, show a larger value of H_0 , or otherwise does not show a preferred direction, we perform our directional analysis. For this, we shall scan the celestial sphere with N spherical caps, of radius γ , and consider two cases: $N = 48$ and $N = 192$ caps.

Let $\Omega_i^\gamma \equiv \Omega(\theta_i, \phi_i, \gamma) \in \mathcal{S}^2$ be a spherical cap on the celestial sphere, of γ degrees of aperture, with vertex at the i th pixel with coordinates (θ_i, ϕ_i) , that is, $(\theta_{\text{cap}}^i, \phi_{\text{cap}}^i) = (\theta_i, \phi_i)$, for $i =$

$1, 2, \dots, N_{\text{pix}}$ (for details of our directional analysis see Bernui et al. [2008]). Both, the number of spherical caps N and the angular coordinates of their centers $\{(\theta_{\text{cap}}^i, \phi_{\text{cap}}^i)\}$, $i = 1, 2, \dots, N$, are defined using the Healpy HEALPix¹ pixelization algorithm [Górski et al., 2005].

The pixelization parameter N_{side} provides the grid resolution that defines the quantity of pixels, N_{pix} , in which the sphere is pixelized

$$N = N_{\text{pix}} = 12 N_{\text{side}}^2, \quad (10)$$

where $N_{\text{side}} = 2^k$, and k is an integer number sometimes called *order*. This means that $N_{\text{side}} = 2$ produces $N = 48$ cap centres, and $N_{\text{side}} = 4$ produces $N = 192$ cap centers, which correspond to the angular resolutions we will use in our directional analysis.

As observed in the lower plot of Figure 1, the SNe are not uniformly distributed on the sky, this is because the Pantheon+ catalog is a compilation of SNe that are short-lived random events in the sky, not long-lived cosmic tracers that can be observed at any time with an astronomical survey. This implies that the number of SNe is not equal in all caps, a fact that we take into account in our error analysis, and in the choice of γ , the radius of the spherical caps.

¹<https://healpy.readthedocs.io/en/latest/>

3.2.1 From the H_0 -caps to the H_0 -map

Our directional analysis consists in calculating H_0 in each one of the N caps that scan the celestial sphere, computation that is done performing the best fit of the HL diagram for the SNe observed in each cap, and assigning the H_0 value found to the centre of the cap. For example, suppose that in the i -th spherical cap, of radius γ , we observe n_i SNe, then we perform the best fit of the HL diagram with these n_i events finding the value H_0^i . In Appendix C, we investigate the correlation between the number of SNe and the best fit H_0 , where we conclude that the number of SNe observed in each of the spherical caps has a negligible impact in the dipolar behaviour of H_0 . The set of N values: $\{H_0^i\}$, for $i = 1, \dots, N$, are then assembled together into a full-sky map, hereafter the H_0 -map; attributing a color scale to these set of real numbers $\{H_0^i\}$ we obtain a colored H_0 -map, as seen in the left panels of Figure 4. The next step is to calculate the dipole component of the H_0 -map, and establish its statistical significance with the help of simulated isotropic maps (see Section 4.3).

The radius of the spherical cap, γ , is a challenge: it cannot be small because the number of SNe observed in that caps would be so small that the best fit is dominated by statistical noise, and cannot be large that one loses precision² in determining the directions where H_0 is maximum or minimum. As a lower limit for the number n_i we consider the number of the SNe analyzed in 1998 [Riess et al., 1998, Perlmutter et al., 1999], that is $n_i \sim 40$ SNe. After various tests, we adopt $\gamma = 60^\circ$. However, we also performed robustness tests with other cap radius to verify that the value $\gamma = 60^\circ$ is not biasing our results. As shown in Appendix D, we redo our directional analysis considering caps with $\gamma = 65^\circ$ and $\gamma = 70^\circ$ obtaining completely similar results.

4 Analyses and Results

In this section, we shall present our analyses and corresponding results. We start calculating the H_0 -maps, for the two angular resolutions, with $N = 48$ and $N = 192$ spherical caps. Then,

we calculate the dipole components of these maps and determine their statistical significance.

4.1 Dipole structure and the angular power spectrum

With all the data in hand, we then calculate the H_0 -maps, scanning the celestial sphere with spherical caps of radius $\gamma = 60^\circ$. Our results are displayed in Figure 4. The next step is to calculate the dipole component C_1 of the corresponding angular power spectra. Clearly, the dipole term C_1 is the larger one, $C_1^{48} = 1.52$ for the H_0 -map⁴⁸ and $C_1^{192} = 1.66$ for the H_0 -map¹⁹², indicating that the H_0 -maps show a net dipolar behavior. However, one needs to evaluate the statistical significance of this result, and this is done by comparison with H_0 -maps obtained by redoing our directional analysis procedure but randomizing the choice of the SNe. The production of these sets of isotropic H_0^{iso} -maps considering 48 and 192 caps, and the statistical analyses to determine the statistical significance of the dipole components of the H_0 -map⁴⁸ and H_0 -map¹⁹² are described in Section 4.3.

We also calculate the direction of the dipole term finding, in galactic coordinates, $(l, b) = (327.^\circ 08 \pm 22.^\circ 5, 28.^\circ 23 \pm 22.^\circ 5)$, for the H_0 -map with $N = 48$ caps, and $(l, b) = (326.^\circ 06 \pm 11.^\circ 2, 27.^\circ 79 \pm 11.^\circ 2)$, for the H_0 -map with $N = 192$ caps. The direction and bulk flow velocity of the dipoles, in the directional analysis with 48 and 192 spherical caps, are summarized in Table 1 (see also Figures 4, 5, and 6).

Regarding the dipole interpretation of our H_0 -maps, we observe in Figure 4 that this is a good approximation, but not an exact result. In fact, the color of each pixel in our H_0 -maps represents the dominance of inflows or outflows, phenomena that increases or decreases the recession speed of matter structures, respectively, relative to the Hubble flow. That is, the diversity of colors in the pixels of a H_0 -map reflects the dominance of one phenomenon or the other, or even the balance between both, effects that are quantified by the best fit H_0^i from the HL diagram of those SNe in the i th cap: reddish (bluish) pixels represent H_0^i values above (below) the mean, and greenish for

²Because including SNe that do not contribute to the direction of interest causes the decrease of the effect we want to measure.

values close to the mean.

Remarkably, the prevalence of each of these phenomena is determined by the large-scale distribution of clustered matter and large voids, and the Local Universe is plenty of them [Courtois et al., 2013, Hoffman et al., 2017, Tully et al., 2023, Dias et al., 2023]. Large matter structures besides the Shapley supercluster, like the South Pole Wall [SPW, Pomarède et al., 2020], a huge structure at $z \simeq 0.04$, produces an inflow that contributes to distort a pure dipolar pattern. On the other hand, the presence of large underdense regions besides the DR [Franco et al., 2024], like the Perseus-Pisces void ($z \simeq 0.027$), is producing outflows that also leave their peculiar signature in our H_0 -maps. All these complex gravitational interactions produce inflows and outflows that affect the dynamics of the SN hosts, phenomena that are captured by our directional analysis and revealed in our H_0 -maps. The observed dipole structure of the H_0 -maps is just the consequence of a dominant gravitational dipole system, i.e., Shapley-DR [Hoffman et al., 2017].

4.2 Bulk flow velocity

Given a data set of low-redshift SNe Ia, $z \ll 1$, one can perform a best fit analysis of the linear HL law and write

$$\left\langle \frac{cz_{\text{CMB}}}{r} \right\rangle = H_0^{b-f}, \quad (11)$$

where the angular parentheses mean the procedure done to obtain the best fit value H_0^{b-f} . Clearly, according to the left panels of Figure 4, the H_0 -maps, the value one obtains in the best fit analysis, H_0^{b-f} , depends on the direction in study. Analyzing these maps one determines the positive (+) and negative (−) dipole directions of the H_0 -maps (right panels of Figure 4). Consider the best fit value of the H_0 -map obtained in the positive (negative) dipole direction, that is, H_0^+ (H_0^-). Then, the directional analysis of the SNe data in these directions, with effective distance R , states

$$\left\langle \frac{cz_{\text{CMB}}}{r} \right\rangle_{\pm} = H_0^{\pm} \simeq H_0 \pm \frac{V_{\text{BF}}(R)}{R}, \quad (12)$$

where we interpret the excess (defect) in H_0 as being the effect of the bulk flow motion, with velocity $V_{\text{BF}}(R)$ at the effective distance R , on the universe expansion rate measured by the SNe. As a consequence of this, one has

$$H_0^+ - H_0^- \equiv \delta H_0(R) \simeq \frac{2V_{\text{BF}}(R)}{R}. \quad (13)$$

Therefore,

$$V_{\text{BF}}(R) \simeq \frac{1}{2}R \delta H_0(R). \quad (14)$$

In what follows we will show how to obtain the effective distance R .

4.2.1 Effective distance R and peculiar velocities

To calculate the effective distance R of a data sample, necessary to compute the bulk flow velocity, we use the thermal noise model of Turnbull et al. [2012],

$$R = \frac{\sum_{i=1}^{N_{\text{SNe}}} D_{Li}/\sigma_i^2}{\sum_{i=1}^{N_{\text{SNe}}} 1/\sigma_i^2}, \quad (15)$$

where D_{Li} is the luminosity distance of the i -th SN, σ_i is the peculiar velocity uncertainty of the i -th SN, and N_{SNe} is the number of SNe in our sample. Unfortunately, the Pantheon+ catalog does not provide uncertainties of the SNe peculiar velocities measurements³. Therefore, for the calculation of the effective distance, R , we need to estimate the set $\{\sigma_i\} = \{\sigma_{v_{\text{pec}i}}\}$.

From equation (2), the peculiar velocity in the radial direction is given by

$$v_{\text{pec}} = cz_{\text{CMB}} - H_0 D_L. \quad (16)$$

To calculate the uncertainty of v_{pec} , $\sigma_{v_{\text{pec}}}$, we use equation (6) multiplied by a factor⁴ $1/\sqrt{2}$, obtaining⁵

$$\sigma_{v_{\text{pec}}} = \frac{1}{\sqrt{2}} \sqrt{D_L^2 \sigma_{H_0}^2 + H_0^2 \sigma_{D_L}^2}. \quad (17)$$

We then compute $\sigma_{v_{\text{pec}}}$ using the best fit values of H_0 and σ_{H_0} , together with D_L and σ_{D_L} , for each SN located in the spherical caps corresponding

³The column of this quantity exists, but the information displayed there is 250 km s^{−1} for all the SNe in the Pantheon+ catalog.

⁴The factor $1/\sqrt{2}$ is an average of all the possible directions of the peculiar velocity, relative to radial direction; see, e.g., Brout et al. [2022].

⁵The uncertainty in the redshift measurements, $\sigma_{z_{\text{CMB}}}$, is negligible.

	$l(^{\circ})$	$b(^{\circ})$	V_{BF} (km s $^{-1}$)	δH_0 (km s $^{-1}$ Mpc $^{-1}$)
$H_0\text{-map}^{48}$	327.08 ± 22.5	28.23 ± 22.5	127.69 ± 110.97	2.44 ± 1.88
$H_0\text{-map}^{192}$	326.06 ± 11.2	27.79 ± 11.2	132.14 ± 109.30	2.57 ± 1.87

Table 1: Bulk flow direction and velocity, for directional analysis with 48 and 192 spherical caps of radius $\gamma = 60^{\circ}$.

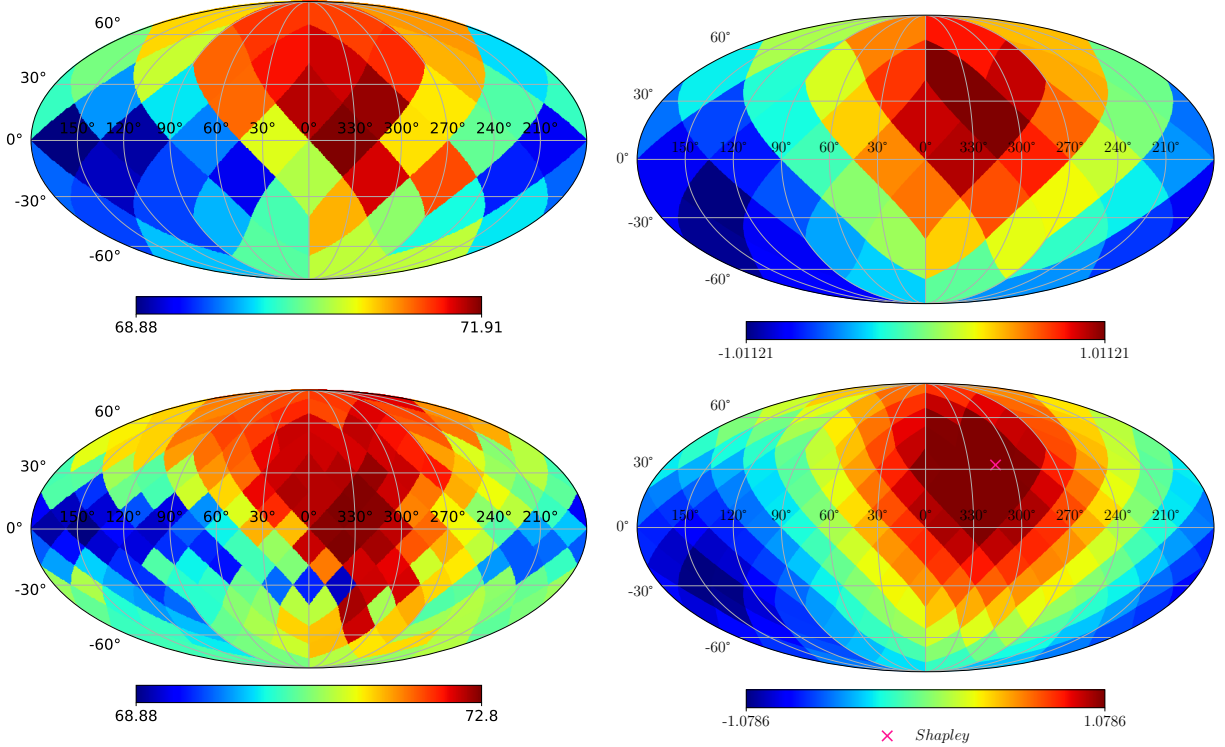


Figure 4: **First row:** the $H_0\text{-map}^{48}$ with resolution $N_{\text{side}} = 2$ (48 spherical caps, left panel), and its dipole component map (right panel). **Second row:** the $H_0\text{-map}^{192}$ with resolution $N_{\text{side}} = 4$ (192 spherical caps, left panel), and its dipole component map (right panel) showing the position of the Shapley supercluster as a multiplication sign X (in fuchsia color) to evidence that the dipole direction obtained in our analyses is very close to this matter structure. Note that all these maps are in units km s $^{-1}$ Mpc $^{-1}$.

to the positive and negative dipole direction of the $H_0\text{-map}$. Performing error propagation, the uncertainty of R , σ_R , is calculated from the uncertainties in the luminosity distance, σ_{DLi} , and in the peculiar velocity, σ_i , that is,

$$\sigma_R = \frac{\sum_{i=1}^{N_{\text{SNe}}} \sigma_{DLi} / \sigma_i^2}{\sum_{i=1}^{N_{\text{SNe}}} 1 / \sigma_i^2}. \quad (18)$$

We then calculate the effective distance using equation (15), and its associated uncertainty using equation (18), obtaining $R^{48} = 104.67 \pm 10.31$ Mpc and $R^{192} = 102.83 \pm 10.24$ Mpc, for $N = 48$ and $N = 192$ spherical caps, respectively. For consistency, we have also estimated the effective distance using Monte Carlo simulations, as

presented in Appendix E, obtaining values fully consistent with these ones.

4.2.2 Bulk flow velocity with SNe Ia

Our measurements of the directional variation of the Hubble constant were done in Section 4.1, where we have obtained a net dipolar structure in the $H_0\text{-maps}$, as seen in Figure 4, with maximum and minimum values $H_0^{\text{max}} = 71.91 \pm 1.42$ and $H_0^{\text{min}} = 68.88 \pm 1.32$ for the $H_0^{48}\text{-map}$, and $H_0^{\text{max}} = 72.80 \pm 1.26$ and $H_0^{\text{min}} = 68.88 \pm 1.17$ for the $H_0^{192}\text{-map}$, respectively (all H_0 values are in units of km s $^{-1}$ Mpc $^{-1}$). The differences among diverse directional measurements of H_0 , observed

in the H_0 -maps shown in the left panels of Figure 4, are interpreted as being originated in the combination of motions of the SNe host galaxies due to the Hubble flow (i.e., the universe expansion) and due to peculiar motions relative to the matter structures, including the bulk flow motion. Clearly, in a universe without peculiar motions, the H_0 -maps should be mono-colour, indicative of the isotropy of H_0 , that is, the same value H_0 in any direction (except statistical fluctuations originated in the best fit procedure of the HL diagrams). According to equation (14), to obtain the magnitude of the bulk flow velocity, we need δH_0 . We calculate $\delta H_0 \equiv H_0^+ - H_0^-$, considering the values in the H_0 -maps (left panels of Figure 4) corresponding to the $+/-$ dipole directions shown in the right panels of Figure 4, obtaining $H_0^{+/48} = 71.78 \pm 1.34$ and $H_0^{-/48} = 69.34 \pm 1.32$, and $H_0^{+/192} = 72.31 \pm 1.34$ and $H_0^{-/192} = 69.74 \pm 1.30$, where all H_0 values are in units of $\text{km s}^{-1} \text{Mpc}^{-1}$. The effective distances, as calculated before, are $R^{48} = 104.67 \pm 10.31 \text{ Mpc}$ and $R^{192} = 102.83 \pm 10.24 \text{ Mpc}$, then

$$V_{\text{BF}48} = \frac{1}{2}(104.67 \pm 10.31)(2.44 \pm 1.88), \quad (19)$$

$$V_{\text{BF}192} = \frac{1}{2}(102.83 \pm 10.24)(2.57 \pm 1.87), \quad (20)$$

finding $V_{\text{BF}48} = 127.81 \pm 110.97 \text{ km s}^{-1}$ and $V_{\text{BF}192} = 132.14 \pm 109.30 \text{ km s}^{-1}$, respectively. Our results are robust, and in good agreement with the values reported in the literature (see Figure 5).

In Figure 6 we can observe some interesting directions on the celestial sphere, including the dipole bulk flow motion found in our analyses. Our results, summarized in Table 1, confirm that the gravitational system Shapley-DR explains well the dipole nature of the bulk flow motion, and that matter structures in the Local Universe appear to move in the direction of the Shapley supercluster with a velocity of $132.14 \pm 109.30 \text{ km s}^{-1}$.⁶

⁶The performance of our approach depends on having a large number of SNe *per* square degree uniformly distributed on the celestial sphere, which is not the present case; in consequence, SNe unevenly distributed on large spherical caps contribute only partially to point out the true bulk flow velocity: the potential contribution \vec{v}_{pec} reduces to its component in the radial direction $v_{pec}^r = \vec{v}_{pec} \cdot \hat{r}$, which can be a small quantity because depends on the angle between \vec{v}_{pec} and the unit vector \hat{r} , angle that can be large, and its *cosine* small, in large spherical caps. As a consequence, our measurement is underestimated.

4.3 Isotropic maps and statistical confidence analysis

We want to verify that the dipole signature found in our H_0 -map analyses is not a biased result, perhaps due to the methodology of analysis, or some artifact in the data. Our statistical confidence test considers the comparison with isotropic H_0 -maps, as follows.

Suppose that the number of SNe in the i th spherical cap is n_i , for $i = 1, \dots, N$. These n_i SNe were selected in the i th cap because their angular separation with respect to the center of the cap is less or equal γ degrees. In this test, instead, for the i th cap we randomly choose n_i SNe from any part of the sky, where $i = 1, \dots, N$; then, we redo the best fit procedure in the N HL diagrams obtaining an isotropic H_0 -map, termed H_0^{Iso} -map. We repeat this process 1000 times, obtaining 1000 H_0^{Iso} -maps. For illustrative purposes, in Figure 7 we show two of these H_0^{Iso} -maps, both for $N = 48$ and 192 spherical caps, i.e., $H_0^{\text{Iso-48}}$ -maps and $H_0^{\text{Iso-192}}$ -maps, respectively. We also calculate the angular coordinates of the dipole components from these H_0^{Iso} -maps, and show them collectively as histograms in Figure 8, again for both angular resolutions, that is, for $N = 48$ and $N = 192$ spherical caps.

Furthermore, we calculate the corresponding dipole component of the H_0^{Iso} -maps in both angular resolutions, $\{C_1^{\text{Iso-48/192}}\}$, useful information to calculate the statistical significance of the dipole components C_1^{48} and C_1^{192} , from the H_0 -map⁴⁸ and H_0 -map¹⁹² (shown in Figure 4), respectively. The distribution of the dipole components from the $H_0^{\text{Iso-48}}$ -maps, $\{C_1^{\text{Iso-48}}\}$, and from the $H_0^{\text{Iso-192}}$ -maps, $\{C_1^{\text{Iso-192}}\}$, as well as the values $C_1^{48} = 1.52$ and $C_1^{192} = 1.66$, are displayed in Figure 9; from these distributions, we obtain the means and standard deviations: $C_1^{\text{Iso-48}} = 0.08$, $C_1^{\text{Iso-192}} = 0.02$ and $\sigma_{\text{Iso-48}} = 0.07$, $\sigma_{\text{Iso-192}} = 0.02$.

In Appendix B we perform Monte Carlo simulations to calculate the uncertainties in C_1^{48} and C_1^{192} , i.e., $\sigma_{C_1^{\text{Ran-48}}} = 0.67$ and $\sigma_{C_1^{\text{Ran-192}}} = 0.35$, respectively. With these data one can finally calcu-

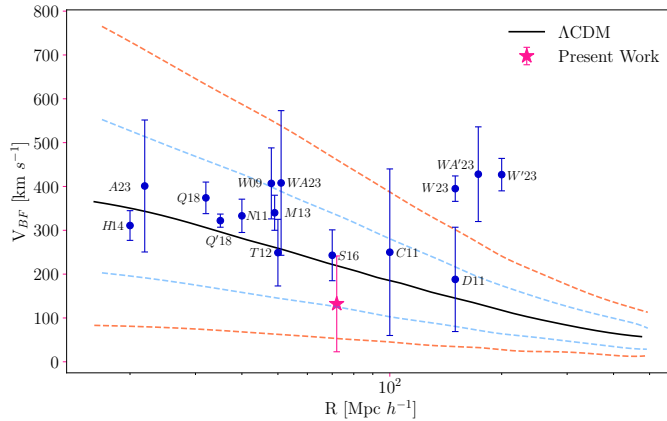


Figure 5: This plot compares several bulk flow velocity measurements with the value expected in the Λ CDM model (continuous line plus 1σ and 2σ limits): A23 [Avila et al., 2023]; H14 [Hong et al., 2014]; Q18 and Q'18 [Qin et al., 2018]; N11 [Nusser and Davis, 2011]; W09 [Watkins et al., 2008]; M13 [Ma and Scott, 2012]; T12 [Turnbull et al., 2012]; S16 [Scrimgeour et al., 2016]; C11 [Colin et al., 2011]; D11 [Dai et al., 2011]; W23 and W'23 [Watkins et al., 2023]; WA23 and WA'23 [Whitford et al., 2023], and the result of our analyses. All effective distances, R , are given in units of $\text{Mpc } h^{-1}$; in this plot, we used $h = 0.7$ for comparison purposes.

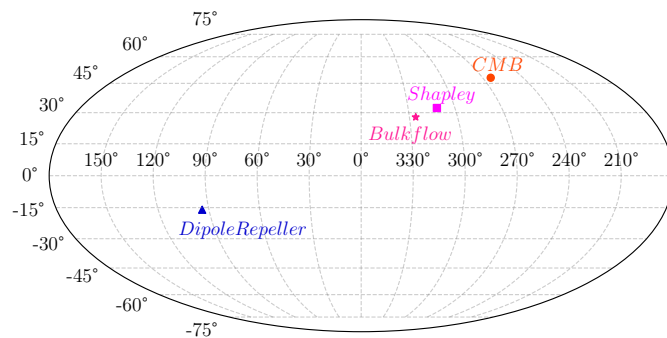


Figure 6: Mollweide projection in galactic coordinates of the structures and directions characterizing flows in the Local Universe: the Dipole Repeller, Shapley supercluster, CMB dipole, and the direction of the bulk flow we found for H_0 -map¹⁹².

late the statistical significance of the dipole components found in our directional analysis; for instance, for the dipole case C_1^{192} one computes the following: $|C_1^{192} - C_1^{\text{Iso-192}}| / \sqrt{\sigma_{C_1^{\text{Ran-192}}}^2 + \sigma_{\text{Iso-192}}^2}$, finding that this dipole is significant at more than 99.9% confidence level.

4.4 Measuring the Hubble constant

Although our directional approach is not intended to perform a H_0 measurement, even so, one can obtain this important information from the monopole components of our H_0 -maps^{48/192}.⁷

This allows us to calculate the Hubble constant at the effective distance $R^{192} = 102.83 \pm 10.24 \text{ Mpc}$, that is, $z \simeq 0.025$, obtaining $H_0 = 70.39 \pm 1.40 \text{ km s}^{-1} \text{ Mpc}^{-1}$ using the H_0 -map¹⁹² and considering spherical caps with $\gamma = 60^\circ$. For completeness, we also calculate for other angular resolutions and spherical cap sizes used in our scrutiny; the results are summarized in Table 2.

In Appendix F we discuss the influence that overdensity and underdensity matter structures can produce on H_0 measurements.

⁷ $H_0 = \sqrt{C_0/4\pi}$, where C_0 is the monopole term of the H_0 -maps.

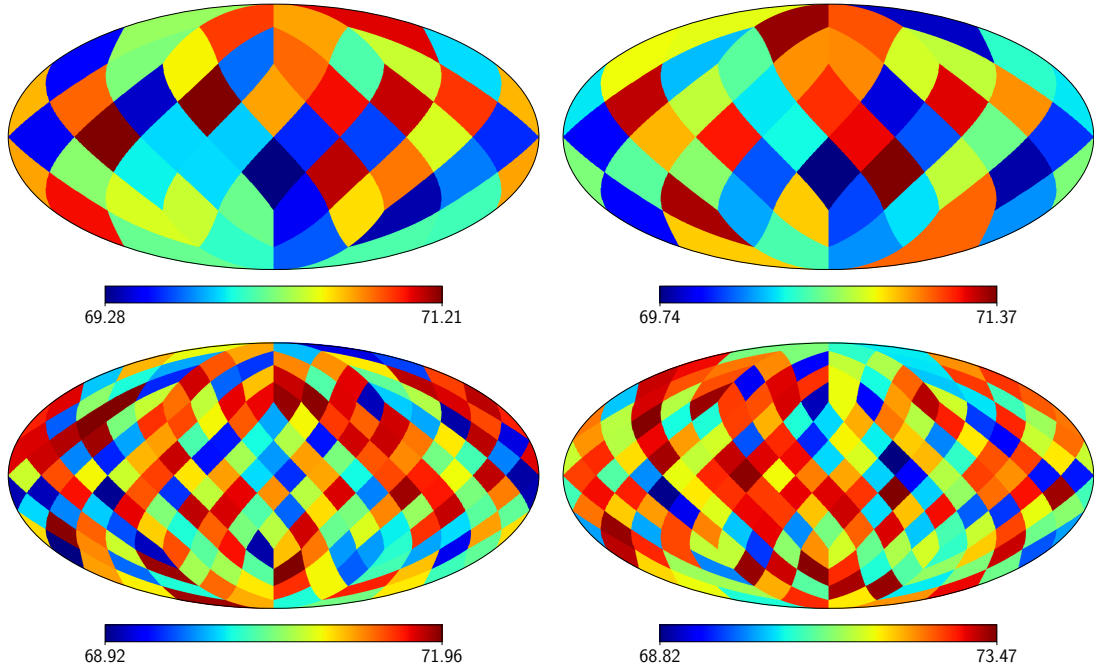


Figure 7: Illustrative examples of simulated isotropic maps, $H_0^{\text{Iso-48}}$ -maps, for $N = 48$ caps (first row), and $H_0^{\text{Iso-192}}$ -maps for $N = 192$ caps (second row).

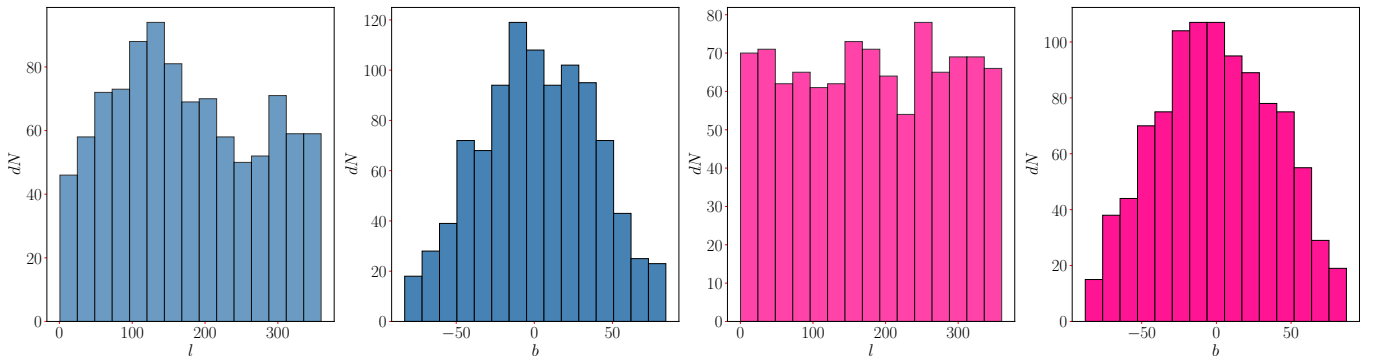


Figure 8: Histogram of the distribution of galactic coordinates l and b , in degrees, for the dipole directions in the generated random H_0^{Iso} -maps. The first and second panels analyze the random maps $H_0^{\text{Iso-48}}$ -map (48 caps), while the third and fourth panels analyze the random maps $H_0^{\text{Iso-192}}$ -map (192 caps). In both cases, our results confirm that the isotropic $H_0^{\text{Iso-48/192}}$ -maps do not exhibit a preferred direction, as expected.

$\gamma \setminus H_0\text{-map}$	H_0 [km s ⁻¹ Mpc ⁻¹]
$\gamma = 60^\circ \setminus H_0\text{-map}^{48}$	70.35 ± 1.50
$\gamma = 60^\circ \setminus H_0\text{-map}^{192}$	70.39 ± 1.40
$\gamma = 65^\circ \setminus H_0\text{-map}^{48}$	70.42 ± 1.45
$\gamma = 65^\circ \setminus H_0\text{-map}^{192}$	70.39 ± 1.27
$\gamma = 70^\circ \setminus H_0\text{-map}^{48}$	70.43 ± 1.38
$\gamma = 70^\circ \setminus H_0\text{-map}^{192}$	70.41 ± 1.18

Table 2: H_0 measurements for different spherical cap sizes.

5 Conclusions

Cosmic matter structures grow over time due to gravitational interaction. This explains why our

cosmic neighborhood, $z \simeq 0$, exhibits amazingly large underdense and overdense matter struc-

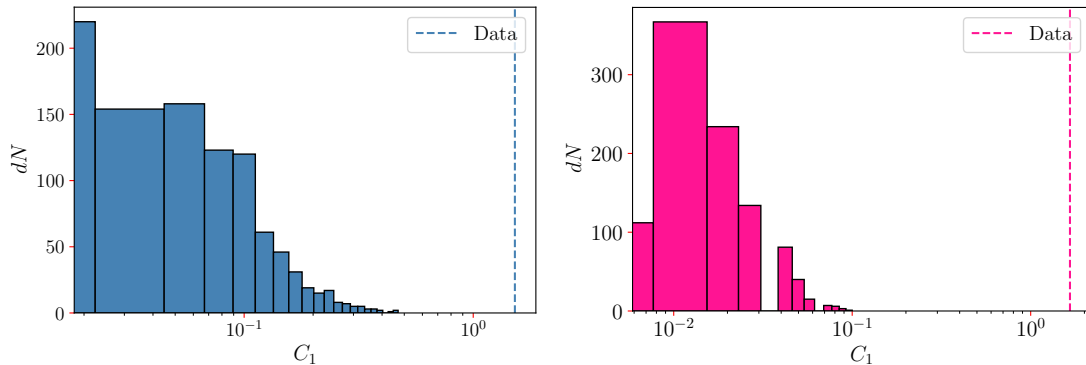


Figure 9: Histograms of the dipole components, C_1 , obtained from 1000 randomized maps, plus the vertical dashed line drawn for comparison from the H_0 -map⁴⁸ (**left panel**) and H_0 -map¹⁹² (**right panel**), with $C_1 = 1.52$ and $C_1 = 1.66$ from the original maps, respectively. As observed, in both cases, our directional analysis shows that the dipole components of the H_0 -maps displayed in Figure 4 are statistically significant, at more than 99.9% confidence level.

tures [Rubin, 1951, de Vaucouleurs, 1953, Courtois et al., 2013, Hoffman et al., 2017, Tully et al., 2019, Colgáin, 2019, de Carvalho et al., 2020, Avila et al., 2021, 2022, Marques et al., 2024]. In this scenario, it was recently proposed that the DR and the Shapley supercluster structures dominate the galaxy velocity field in the Local Universe, acting like a dipolar gravitational system. This scenario deserves investigation because in the Local Universe the effect of peculiar motions caused by the distribution of matter competes with the expansion of the universe making the analysis of the HL diagram difficult, affecting the measurement of the Hubble constant.

Motivated by this proposal, we investigated the subsample of 501 SNe Ia of the Pantheon+ catalog in the Local Universe, with redshifts $0.015 \leq z \leq 0.06$, aiming to measure both the direction and magnitude of the bulk flow velocity. Our directional analysis scans the celestial sphere considering two angular resolutions: with $N = 48$ and $N = 192$ spherical caps, although our conclusions are drawn from the best angular resolution case, i.e., for $N = 192$ caps. We found a statistically significant dipole variation of the Hubble constant, at more than 99.9% confidence level, with H_0 values in the \pm dipole directions: $H_0^{+/192} = 72.31 \pm 1.34 \text{ km s}^{-1} \text{ Mpc}^{-1}$ and $H_0^{-/192} = 69.74 \pm 1.30 \text{ km s}^{-1} \text{ Mpc}^{-1}$, for the H_0^{192} -map. The Table 1, and Figures 4 and 5, summarize our results.

Our studies confirm that matter structures

in the Local Universe are indeed following a dipolar bulk flow motion toward $(l, b) = (326.^\circ 1 \pm 11.^\circ 2, 27.^\circ 8 \pm 11.^\circ 2)$, a direction close to the Shapley supercluster $(l_{\text{Shapley}}, b_{\text{Shapley}}) = (311.53^\circ, 32.31^\circ)$, with the velocity of $132.14 \pm 109.30 \text{ km s}^{-1}$ at the effective distance $102.83 \pm 10.24 \text{ Mpc} = 71.98 \pm 7.17 \text{ Mpc } h^{-1}$, using $h = 0.7$ to illustrate the measurements' comparison shown in Figure 5.

Not less interesting, the antipodal direction of the dipolar bulk flow found points close to the DR structure, as illustrated in Figure 6.

As shown in Figure 5, recent studies of the CosmicFlows-4 data [CF4, Tully et al., 2023] at scales greater than $100 \text{ Mpc } h^{-1}$ have reported bulk flow velocities that are in great tension with the velocities expected in the standard cosmological model, like the measurements of Watkins et al. [2023] who found $395 \pm 29 \text{ km s}^{-1}$ at $150 \text{ Mpc } h^{-1}$ and $427 \pm 37 \text{ km s}^{-1}$ at $200 \text{ Mpc } h^{-1}$, and the measurement of Whitford et al. [2023] who found $428 \pm 108 \text{ km s}^{-1}$ at $173 \text{ Mpc } h^{-1}$, values with very low probability of occurrence: 0.015%, 0.00015%, and 0.11%, respectively (these data are also displayed in Figure 5). As suggested by Watkins et al. [2023], these results may be an indication that the matter rest frame of the universe is not that determined from the dipole in the CMB radiation [see, e.g., Migkas et al., 2021].

However, several analyses performed at moderate scales $\lesssim 100 \text{ Mpc } h^{-1}$ estimate the bulk flow velocities finding that they are statistically

consistent with the Λ CDM prediction, as well as the measurement of Whitford et al. [2023] at 49 Mpc h^{-1} analysing the CF4 dataset, and also our measurement at the effective distance of 72 Mpc h^{-1} .

Concluding, our directional analysis shows that the bulk flow velocity field in the Local Uni-

verse is well explained by the gravitational dipole system *Shapley-DR* [Hoffman et al., 2017]. In addition, we are confident that our results are robust, and the methodology adopted is unbiased due to the various consistency tests done, which we present in Appendix.

Acknowledgments

M.L., C.F., and A.B. acknowledge to CAPES and CNPq for their corresponding fellowships. F.A. thanks CNPq and FAPERJ, Processo SEI 260003/014913/2023, for financial support.

A Consistency test for other redshift intervals

We have investigated the consistency of our results studying the SNe present in other redshift intervals, close to the original interval analyzed in this work. Thus, we performed our directional analysis for four SNe samples with redshift intervals as follows: $z \in [0.01, 0.06]$, $z \in [0.01, 0.055]$, $z \in [0.01, 0.065]$, and $z \in [0.015, 0.065]$; the number of SNe Ia in these intervals was 565, 552, 576, and 512, respectively. The H_0 -maps¹⁹² obtained in each case are displayed in the left column of Figure 10. To illustrate how different these maps are with respect to the original H_0 -map¹⁹², analyzed for the SNe with $z \in [0.015, 0.06]$ and displayed in the left panel, second row, of Figure 4, we calculate the map difference $D^i \equiv [H_0\text{-map}^{192/\text{orig}} - H_0\text{-map}^{192/i}]$, where the index i refers to each one of the four samples mentioned above. The maps $\{D^i\}$, displayed in the right column of Figure 10, show that the differences with respect to $H_0\text{-map}^{192/\text{orig}}$ are very tiny for the first two cases, and differences $\lesssim 2\%$ for the last two cases, implying that our results regarding the interval analyzed in this work, $z \in [0.015, 0.06]$, are robust.

B Uncertainty Due to the Dipole δH_0 : Monte Carlo Simulations

The dipolar nature of $\delta H_0(l, b)$ contributes to the uncertainty in the measurement of H_0^{b-f} (see Section 3.1.2). To calculate this uncertainty, σ_{dp} , due to the directional dependence observed in $H_0^{b-f}(l, b)$, we perform Monte Carlo simulations.

We first generate 1000 random samples of SNe, where their angular positions (l, b) were preserved, but their luminosity distances were estimated randomly from a Gaussian distribution, considering, as the mean and the standard deviation of such distribution, the luminosity distance of each SN D_L , and its uncertainty σ_{D_L} , respectively. We then performed the same process of directional analysis considering both angular resolutions, that is, with $N = 48$ and $N = 192$ caps. Then, performing the H_0 best fit procedure in the HL diagrams, we obtain 1000 random H_0 -maps^{Ran-48} and 1000 random H_0 -maps^{Ran-192}.⁸

For each one of these maps, we calculate the amplitudes $\{\delta H_0\}^{\text{Ran-48}/192}$, the dipole components $\{C_1\}^{\text{Ran-48}/192}$, and the dipole directions $\{(l, b)\}^{\text{Ran-48}/192}$. The corresponding histograms of the distributions obtained are shown in Figure 11 (the first and second rows correspond to $N = 48$, and the third and fourth rows correspond to $N = 192$). The standard deviation of the distributions $\{\delta H_0\}^{\text{Ran-48}/192}$ provides a measure of the uncertainty due to the dipole nature of the H_0 -map, δH_0 , where we obtain $\sigma_{dp}^{48} = 1.26 \text{ km s}^{-1} \text{ Mpc}^{-1}$ and $\sigma_{dp}^{192} = 1.24 \text{ km s}^{-1} \text{ Mpc}^{-1}$, respectively.

Another quantity that we analyze in Figure 11 are the set of dipole components $\{C_1\}^{\text{Ran-48}/192}$ of the $H_0^{\text{Ran-48}/192}$ -maps, where their standard deviations provide a measurement of the uncertainties in

⁸Not to be confused with the isotropic $H_0^{\text{Iso-48}/192}$ -maps, see Section 4.3.

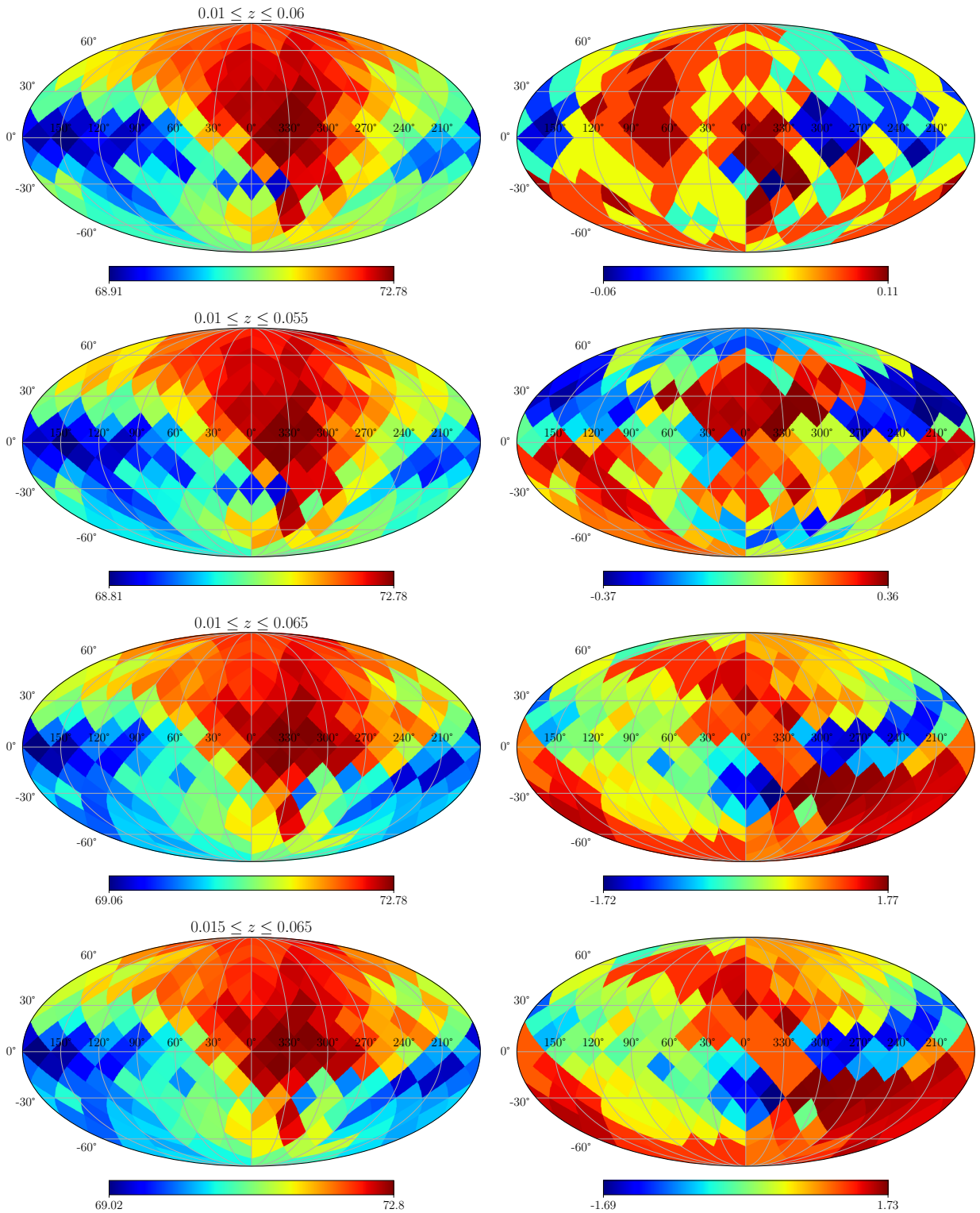


Figure 10: **Left column:** the H_0 -maps¹⁹² for different redshift intervals. **Right column:** the maps of the difference between the original H_0 -map¹⁹² (see Figure 4) and the corresponding map to the left.

the dipole components C_1^{48} and C_1^{192} of our H_0 -maps (shown in Figure 4), obtaining $\sigma_{C_1^{\text{Ran-48}}} = 0.67$ and $\sigma_{C_1^{\text{Ran-192}}} = 0.35$, respectively. These quantities are used to estimate the statistical significance of the dipole nature of our results (see Section 4.3).

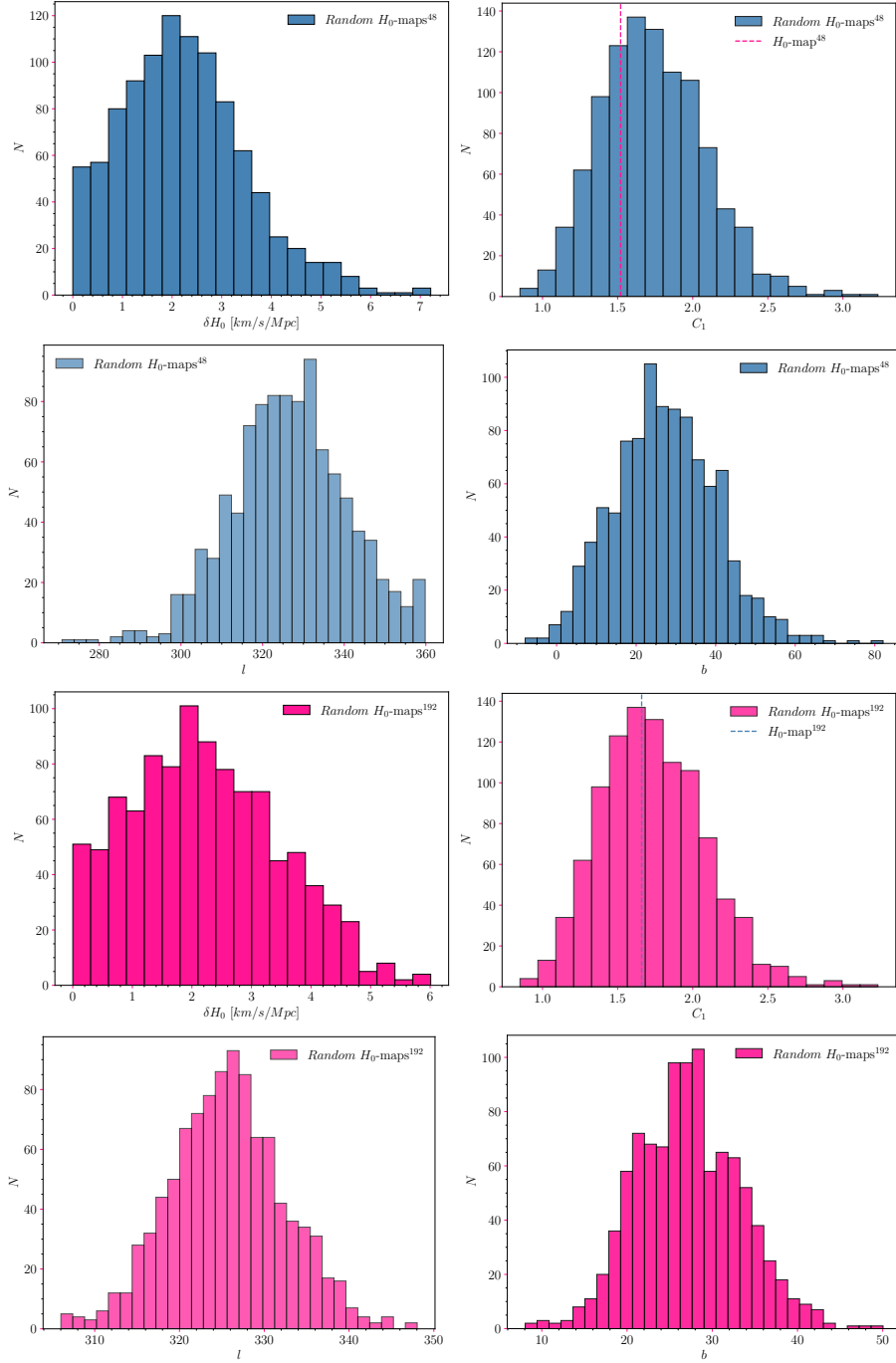


Figure 11: These plots show the results of our Monte Carlo simulations performed to produce H_0 -maps^{Ran-48/192} from which one can estimate the uncertainties of quantities used in our approach. In the first row we display the amplitudes $\{\delta H_0\}^{\text{Ran-48}}$ (left panel) and the dipole component $\{C_1\}^{\text{Ran-48}}$ (right panel) calculated from random H_0 -maps^{Ran-48}, where their standard deviations provide the uncertainties $\sigma_{dp}^{48} = 1.26 \text{ km s}^{-1} \text{ Mpc}^{-1}$, and $\sigma_{C_1^{\text{Ran-48}}} = 0.67$, respectively (see Appendix B for details). The third row show similar calculations, but for the $N = 192$ case, namely, $\sigma_{dp}^{192} = 1.24 \text{ km s}^{-1} \text{ Mpc}^{-1}$, and $\sigma_{C_1^{\text{Ran-192}}} = 0.35$. The second and fourth rows provide the distributions of the dipole directions of the H_0 -maps^{Ran-48/192}, showing mean and standard deviations as expected due to the procedure used in these Monte Carlo simulations, that is, $(l, b)^{\text{Ran-48}} = (326.^{\circ}58 \pm 14.^{\circ}33, 27.^{\circ}33 \pm 12.^{\circ}76)$ and $(l, b)^{\text{Ran-192}} = (325.^{\circ}68 \pm 6.^{\circ}76, 27.^{\circ}17 \pm 6.^{\circ}1)$. The vertical dashed lines in the $\{C_1\}^{\text{Ran-48/192}}$ plots (right panels in the first and third row) represent the dipole values $C_1^{48} = 1.52$ and $C_1^{192} = 1.66$ of the H_0 -maps displayed in Figure 4 (see Section 4.3 and Figure 9).

C Studying the correlation between the number of SNe and the best fit H_0

An interesting question regards the possible bias of the number of SNe observed in different directions could have an impact in the best fit analysis of the HL diagram to obtain H_0 .

For this, we perform a correlation analysis of the H_0 -map with the number-of-SNe-map (that is, the map where the color in each pixel represents the number of SNe used to construct our H_0 -map, see Figure 12), using the linear Pearson correlation coefficient \mathcal{P} . Our analyses show (the bars mean absolute value): $|\mathcal{P}| = 0.234$, for the case with $N = 48$ spherical caps, and $|\mathcal{P}| = 0.198$, for the case with $N = 192$ spherical caps. According to the literature, for values of the Pearson coefficient in the interval, $|\mathcal{P}| \in [0.0, 0.199]$ means that the correlation between the pairs of maps with the same angular resolution is *very weak*.

Notice that, for consistency, our analyses scan the celestial sphere considering two angular resolutions: with $N = 48$ and with $N = 192$ spherical caps. However, our conclusions are drawn from the best angular resolution case, i.e., scanning the celestial sphere with $N = 192$ spherical caps. Due to this, we are led to conclude that the number of SNe observed in the 192 spherical caps has a negligible impact in the –statistically significant–dipolar behavior that our directional analysis found in the H_0 -map.

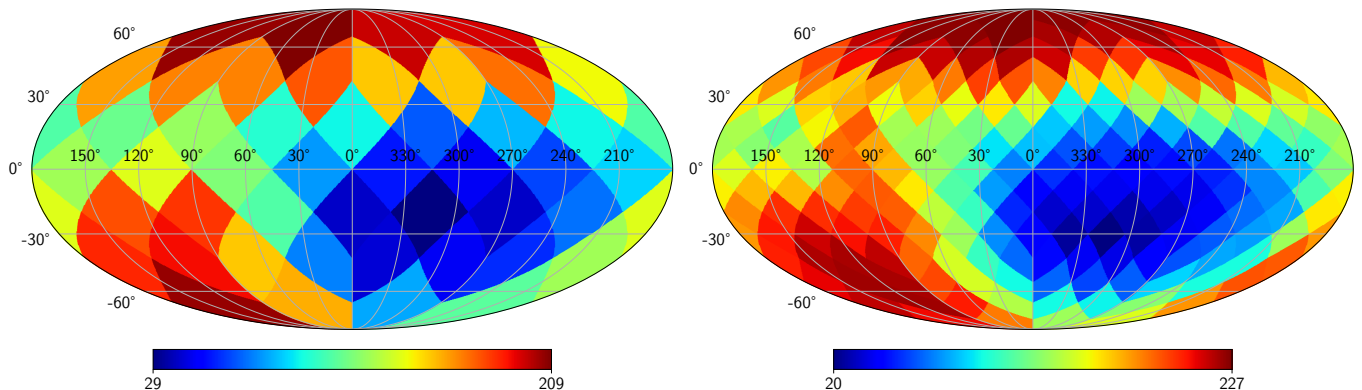


Figure 12: Number of SNe maps, for 48 (left) and 192 (right) spherical caps analyses. These maps show the number of SNe analyzed in each spherical cap, as in the directional analysis procedure, by assigning a color to the corresponding number of SNe inside the 60° cap. These maps are useful to study the possible correlation with the maps shown in Figure 4; our results, discussed in Appendix C, confirm that the correlation is very weak.

D Robustness for Other Spherical Cap Sizes: $\gamma = 65^\circ, 70^\circ$

In this appendix, we perform robustness tests to verify our directional analyses results considering spherical caps with radius different from $\gamma = 60^\circ$, the case considered along this work, namely $\gamma = 65^\circ$ and $\gamma = 70^\circ$. Moreover, we make these tests for both angular resolutions, with 48 and 192 spherical caps.

Observing Table 3, and the H_0 -maps displayed in Figure 13, we obtain an excellent agreement with the results found along the text considering spherical caps with $\gamma = 60^\circ$. Therefore, we conclude that our results, summarized in Table 1, are robust considering directional analysis done with spherical caps of different sizes used to scan the celestial sphere.

E Consistency in the Calculation of the Effective Distance

The calculation of the effective distance is an important step in our methodology of finding the velocity of the bulk flow. Equation (15) is based on the thermal noise model of Turnbull et al. [2012],

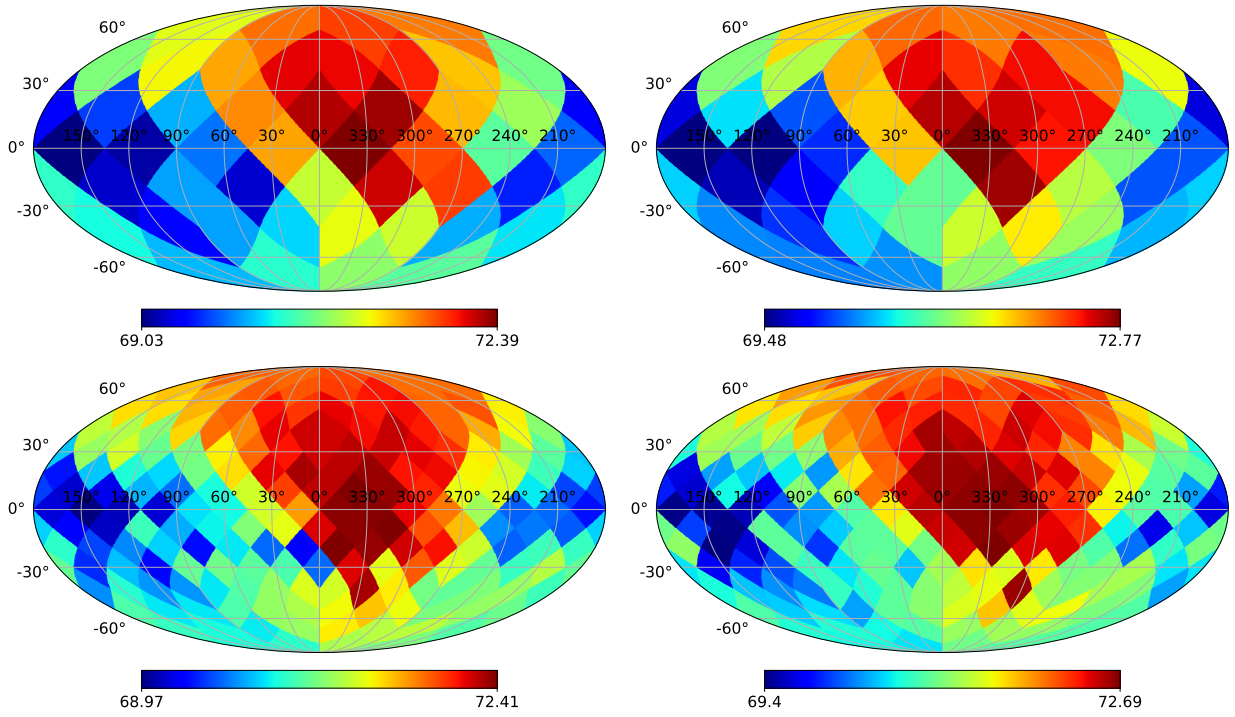


Figure 13: Robustness tests to confirm our directional analysis results considering different spherical cap sizes, namely: $\gamma = 65^\circ$ and $\gamma = 70^\circ$, tests done for both angular resolutions, with 48 and 192 spherical caps. The plots at the top correspond to the cases with 48 caps for $\gamma = 65^\circ$ (left) and $\gamma = 70^\circ$ (right). The plots at the bottom correspond to the cases with 192 caps for $\gamma = 65^\circ$ (left) and $\gamma = 70^\circ$ (right). As observed, comparing the dipole directions of these H_0 -maps, displayed in Table 3, with those in Table 1 both results are in excellent agreement.

	$l(^{\circ})$	$b(^{\circ})$
$H_0\text{-map}^{48} / \gamma = 65^{\circ}$	323.87 ± 22.5	28.04 ± 22.5
$H_0\text{-map}^{192} / \gamma = 65^{\circ}$	328.25 ± 11.2	27.42 ± 11.2
$H_0\text{-map}^{48} / \gamma = 70^{\circ}$	323.87 ± 22.5	28.04 ± 22.5
$H_0\text{-map}^{192} / \gamma = 70^{\circ}$	326.63 ± 11.2	29.77 ± 11.2

Table 3: Robustness tests to verify our directional analysis results considering different spherical cap sizes.

that needs the information of the peculiar velocities’ uncertainties, which are individually unknown in the Pantheon+ catalog, and just appears as value 250 km s^{-1} for all SNe.

In Section 4.2.1, we have calculated $\sigma_{v_{pec}}$ using Equation (17). However, one can adopt the Monte Carlo method to find $\sigma_{v_{pec}}$ and the effective distance R . For this, we simulate Gaussian distributions for each SN located within the spherical caps corresponding to both the $+/-$ dipole directions (see Table 1), considering the value v_{pec}^i (data in the Pantheon+ catalog) as the mean of the distribution and 250 km s^{-1} as its standard deviation. For each distribution, one for each SN in the analysis, we randomly choose a value that we consider the uncertainty $\sigma_{v_{pec}}$ of such SN. The set of values $\{\sigma_{v_{pec}}\}$ obtained in this form is termed one realization. With this set of uncertainties, we calculate the value of the effective distance R using Equation (15) for each realization.

We repeat this procedure to produce a set of $N_{\text{realiz}} = 5000$ realizations⁹, for each angular resolution, that is, for 48 and 192 spherical caps. The set of effective distances obtained $\{R_j\}, j = 1, \dots, 5000$ produces two distributions for 48 and 192 caps, respectively, that we plot as histograms in Figure 14. The median of these distributions provides the value of the effective distance R . Therefore, we obtain $R^{48} = 118.33 \pm 33.71 \text{ Mpc}$, and $R^{192} = 117.57 \pm 33.60 \text{ Mpc}$, results that are in good agreement with those found in Section 4.2.1, with larger uncertainties than previous ones.

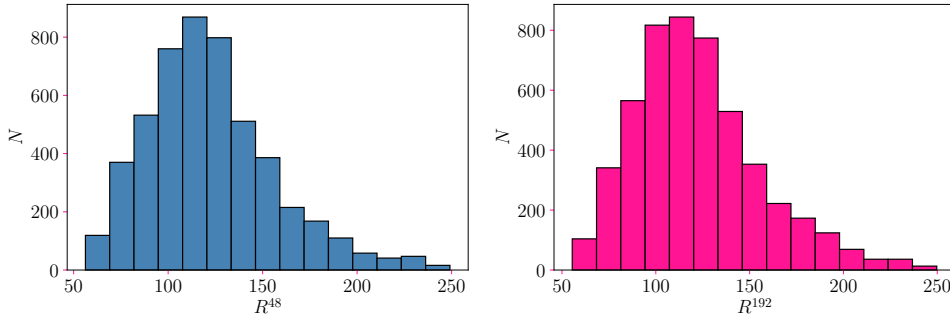


Figure 14: Histograms of the distributions obtained using the Monte Carlo approach (see the text for details) to calculate the effective distance R , in units of Mpc, for $H_0\text{-map}^{48}$ (left panel) and $H_0\text{-map}^{192}$ (right panel). The median values of these distributions, that provide our measurements of R , are: $R^{48} = 118.33 \pm 33.71 \text{ Mpc}$, and $R^{192} = 117.57 \pm 33.60 \text{ Mpc}$, respectively.

F The Hubble Tension: Are Overdensities and Underdensities Biasing the H_0 Measurements?

Recent works [Giani et al., 2024, Mazurenko et al., 2024, Kenworthy et al., 2019] have investigated the possibility that overdensities (i.e., large galaxy clusters) and underdensities (i.e., large voids) affect the H_0 measurements in the Local Universe, because such structures produce large inflows and outflows, respectively. In fact, this biasing effect exists, being important quantify the impact of such phenomena

⁹We verified that for a greater number of realizations the final value of the effective distance R remains practically the same.

in the measurements of H_0 . According to [Giani et al. \[2024\]](#), the large supercluster Laniakea, which hosts the Milky Way, produces a negative average expansion of $\sim -1.1 \text{ km s}^{-1} \text{ Mpc}^{-1}$, inducing a variation in the Hubble constant $\Delta H_0 \approx 0.5 \text{ km s}^{-1} \text{ Mpc}^{-1}$. Therefore, the inflows produced by Laniakea can increase the Hubble tension when applying this correction to the SNe Ia dataset. On the other hand, [Mazurenko et al. \[2024\]](#) noticed that a large supervoid could be generating outflows on scales $100 - 250 \text{ Mpc } h^{-1}$ inducing a change in the bulk flow velocities at such scales, then decreasing the tension due to the measurements reported by [Watkins et al. \[2023\]](#) and [Whitford et al. \[2023\]](#); data that we commented at the end of Section 5. Lastly, [Kenworthy et al. \[2019\]](#) affirm that overdensities and underdensities can change the Hubble constant in 2.2%, not affecting the Hubble tension.

In this context, our directional analysis can didactically explain these results, and also provide a quantification of this biasing effect. The color of each pixel in our H_0 -maps (see, e.g., the left column in Figure 4) is the manifestation of the dominance of inflows or outflows, phenomena that increases or decreases the recession speed of matter structures with respect to the Hubble flow. In fact, the prevalence of these phenomena in the Local Universe is determined by the large-scale distribution of clustered matter and large voids, which can vary substantially along different directions as recently noticed by [Franco et al. \[2024\]](#). However, this diversity is captured by our methodology, which provides, for the i th spherical cap in analysis, the best fit H_0^i from the HL diagram of those SNe in the i th cap; since the i th cap has its vertex at the position of pixel i , it will have the color corresponding to the dominant effect in that direction: reddish (bluish) for values above (below) the mean, and greenish for values close to the mean. The relative differences of the pixel values of the H_0 -map with respect to the H_0 value shown in Table 2 are $\lesssim 3\%$ in all cases, i.e., considering different angular resolutions and cap sizes, in perfect agreement with the outcomes of [Kenworthy et al. \[2019\]](#).

References

- F. Avila, C. P. Novaes, A. Bernui, E. de Carvalho, and J. P. Nogueira-Cavalcante. The angular scale of homogeneity in the local Universe with the SDSS blue galaxies. *mnras*, 488(1):1481–1487, Sept. 2019. doi: 10.1093/mnras/stz1765.
- F. Avila, A. Bernui, E. de Carvalho, and C. P. Novaes. The growth rate of cosmic structures in the local Universe with the ALFALFA survey. *mnras*, 505(3):3404–3413, Aug. 2021. doi: 10.1093/mnras/stab1488.
- F. Avila, A. Bernui, R. C. Nunes, E. de Carvalho, and C. P. Novaes. The homogeneity scale and the growth rate of cosmic structures. *mnras*, 509(2):2994–3003, Jan. 2022. doi: 10.1093/mnras/stab3122.
- F. Avila, J. Oliveira, M. L. S. Dias, and A. Bernui. The bulk flow motion and the Hubble-Lemaître law in the Local Universe with the ALFALFA survey. *Brazilian Journal of Physics*, 53:49, Feb. 2023. doi: 10.1007/s13538-023-01259-z.
- D. Baumann. *Cosmology*. Cambridge University Press, 7 2022. ISBN 978-1-108-93709-2, 978-1-108-83807-8. doi: 10.1017/9781108937092.
- A. Bernui, I. S. Ferreira, and C. A. Wuensche. On the Large-Scale Angular Distribution of Short Gamma-Ray Bursts. *apj*, 673(2):968–971, Feb. 2008. doi: 10.1086/524678.
- D. Brout, D. Scolnic, B. Popovic, A. G. Riess, A. Carr, J. Zuntz, R. Kessler, T. M. Davis, S. Hinton, D. Jones, W. D. Kenworthy, E. R. Peterson, K. Said, G. Taylor, N. Ali, P. Armstrong, P. Charvu, A. Dwomoh, C. Meldorf, A. Palmese, H. Qu, B. M. Rose, B. Sanchez, C. W. Stubbs, M. Vincenzi,

- C. M. Wood, P. J. Brown, R. Chen, K. Chambers, D. A. Coulter, M. Dai, G. Dimitriadis, A. V. Filippenko, R. J. Foley, S. W. Jha, L. Kelsey, R. P. Kirshner, A. Möller, J. Muir, S. Nadathur, Y.-C. Pan, A. Rest, C. Rojas-Bravo, M. Sako, M. R. Siebert, M. Smith, B. E. Stahl, and P. Wiseman. The Pantheon+ Analysis: Cosmological Constraints. *ApJ*, 938(2):110, Oct. 2022. doi: 10.3847/1538-4357/ac8e04.
- P. Coles. The large-scale structure of the universe. *Contemporary Physics*, 37(6):429–440, 1996. doi: 10.1080/00107519608217534. URL <https://doi.org/10.1080/00107519608217534>.
- E. Ó. Colgáin. A hint of matter underdensity at low z ? *jcap*, 9(9):006, Sept. 2019. doi: 10.1088/1475-7516/2019/09/006.
- J. Colin, R. Mohayaee, S. Sarkar, and A. Shafieloo. Probing the anisotropic local Universe and beyond with SNe Ia data. *Monthly Notices of the Royal Astronomical Society*, 414(1):264–271, 06 2011. ISSN 0035-8711. doi: 10.1111/j.1365-2966.2011.18402.x. URL <https://doi.org/10.1111/j.1365-2966.2011.18402.x>.
- S. Courteau and S. van den Bergh. The Solar Motion Relative to the Local Group. *aj*, 118(1):337–345, July 1999. doi: 10.1086/300942.
- H. M. Courtois, D. Pomarède, R. B. Tully, Y. Hoffman, and D. Courtois. Cosmography of the Local Universe. *aj*, 146(3):69, Sept. 2013. doi: 10.1088/0004-6256/146/3/69.
- D.-C. Dai, W. H. Kinney, and D. Stojkovic. Measuring the cosmological bulk flow using the peculiar velocities of supernovae. *Journal of Cosmology and Astroparticle Physics*, 2011(04):015, apr 2011. doi: 10.1088/1475-7516/2011/04/015. URL <https://dx.doi.org/10.1088/1475-7516/2011/04/015>.
- E. de Carvalho, A. Bernui, H. S. Xavier, and C. P. Novaes. Baryon acoustic oscillations signature in the three-point angular correlation function from the SDSS-DR12 quasar survey. *mnras*, 492(3):4469–4476, Mar. 2020. doi: 10.1093/mnras/staa119.
- V. de Lapparent, M. J. Geller, and J. P. Huchra. A Slice of the Universe. *apjl*, 302:L1, Mar. 1986. doi: 10.1086/184625.
- G. de Vaucouleurs. Evidence for a local supergalaxy. *aj*, 58:30, Feb. 1953. doi: 10.1086/106805.
- B. L. Dias, F. Avila, and A. Bernui. Probing cosmic homogeneity in the Local Universe. *mnras*, 526(3):3219–3229, Dec. 2023. doi: 10.1093/mnras/stad2980.
- C. Franco, F. Avila, and A. Bernui. Probing cosmic isotropy in the Local Universe. *mnras*, 527(3):7400–7413, Jan. 2024. doi: 10.1093/mnras/stad3616.
- L. Giani, C. Howlett, K. Said, T. Davis, and S. Vagnozzi. An effective description of Laniakea: impact on cosmology and the local determination of the Hubble constant. *jcap*, 2024(1):071, Jan. 2024. doi: 10.1088/1475-7516/2024/01/071.
- K. M. Górski, E. Hivon, A. J. Banday, B. D. Wandelt, F. K. Hansen, M. Reinecke, and M. Bartelmann. HEALPix: A Framework for High-Resolution Discretization and Fast Analysis of Data Distributed on the Sphere. *ApJ*, 622(2):759–771, Apr. 2005. doi: 10.1086/427976.
- S. A. Gregory and L. A. Thompson. The Coma/A1367 supercluster and its environs. *apj*, 222:784–799, June 1978. doi: 10.1086/156198.
- Y. Hoffman, D. Pomarède, R. B. Tully, and H. M. Courtois. The dipole repeller. *Nature Astronomy*, 1:0036, Jan. 2017. doi: 10.1038/s41550-016-0036.

- T. Hong, C. M. Springob, L. Staveley-Smith, M. I. Scrimgeour, K. L. Masters, L. M. Macri, B. S. Koribalski, D. H. Jones, and T. H. Jarrett. 2MTF - IV. A bulk flow measurement of the local Universe. *mnras*, 445(1):402–413, Nov. 2014. doi: 10.1093/mnras/stu1774.
- N. Kaiser. Clustering in real space and in redshift space. *mnras*, 227:1–21, July 1987. doi: 10.1093/mnras/227.1.1.
- B. Kalbouneh, C. Marinoni, and J. Bel. Multipole expansion of the local expansion rate. *prd*, 107(2):023507, Jan. 2023. doi: 10.1103/PhysRevD.107.023507.
- W. D. Kenworthy, D. Scolnic, and A. Riess. The Local Perspective on the Hubble Tension: Local Structure Does Not Impact Measurement of the Hubble Constant. *apj*, 875(2):145, Apr. 2019. doi: 10.3847/1538-4357/ab0ebf.
- C. E. Kester, A. Bernui, and W. S. Hipólito-Ricaldi. Probing the statistical isotropy of the universe with Planck data of the cosmic microwave background. *aap*, 683:A176, Mar. 2024. doi: 10.1051/0004-6361/202348160.
- D. Lynden-Bell, S. M. Faber, D. Burstein, R. L. Davies, A. Dressler, R. J. Terlevich, and G. Wegner. Photometry and Spectroscopy of Elliptical Galaxies. V. Galaxy Streaming toward the New Supergalactic Center. *apj*, 326:19, Mar. 1988. doi: 10.1086/166066.
- Y.-Z. Ma and D. Scott. Cosmic bulk flows on $50h^{-1}$ Mpc scales: a Bayesian hyper-parameter method and multishell likelihood analysis. *Monthly Notices of the Royal Astronomical Society*, 428(3):2017–2028, 11 2012. ISSN 0035-8711. doi: 10.1093/mnras/sts178. URL <https://doi.org/10.1093/mnras/sts178>.
- G. A. Marques, C. P. Novaes, A. Bernui, and I. S. Ferreira. Isotropy analyses of the Planck convergence map. *mnras*, 473(1):165–172, Jan. 2018. doi: 10.1093/mnras/stx2240.
- G. A. Marques, J. Liu, M. Shirasaki, L. Thiele, D. Grandón, K. M. Huffenberger, S. Cheng, J. Harnois-Déraps, K. Osato, and W. R. Coulton. Cosmology from weak lensing peaks and minima with Subaru Hyper Suprime-Cam Survey first-year data. *mnras*, 528(3):4513–4527, Mar. 2024. doi: 10.1093/mnras/stae098.
- S. Mazurenko, I. Banik, P. Kroupa, and M. Haslbauer. A simultaneous solution to the Hubble tension and observed bulk flow within $250 h^{-1}$ Mpc. *mnras*, 527(3):4388–4396, Jan. 2024. doi: 10.1093/mnras/stad3357.
- R. Mc Conville and E. Ó Colgáin. Anisotropic distance ladder in Pantheon+supernovae. *prd*, 108(12):123533, Dec. 2023. doi: 10.1103/PhysRevD.108.123533.
- K. Migkas, F. Pacaud, G. Schellenberger, J. Erler, N. T. Nguyen-Dang, T. H. Reiprich, M. E. Ramos-Ceja, and L. Lovisari. Cosmological implications of the anisotropy of ten galaxy cluster scaling relations. *aap*, 649:A151, May 2021. doi: 10.1051/0004-6361/202140296.
- A. Nusser and M. Davis. The Cosmological Bulk Flow: Consistency with Λ CDM and $z \approx 0$ Constraints on σ_8 and γ . *apj*, 736(2):93, Aug. 2011. doi: 10.1088/0004-637X/736/2/93.
- P. J. E. Peebles. *The large-scale structure of the universe*. Princeton University Press, 1980.
- L. Perivolaropoulos. Isotropy properties of the absolute luminosity magnitudes of SNIa in the Pantheon + and SH0ES samples. *prd*, 108(6):063509, Sept. 2023. doi: 10.1103/PhysRevD.108.063509.
- S. Perlmutter et al. Measurements of Ω and Λ from 42 high redshift supernovae. *Astrophys. J.*, 517:565–586, 1999. doi: 10.1086/307221.

- E. R. Peterson, W. D. Kenworthy, D. Scolnic, A. G. Riess, D. Brout, A. Carr, H. Courtois, T. Davis, A. Dwomoh, D. O. Jones, B. Popovic, B. M. Rose, and K. Said. The Pantheon+ Analysis: Evaluating Peculiar Velocity Corrections in Cosmological Analyses with Nearby Type Ia Supernovae. *apj*, 938(2):112, Oct. 2022. doi: 10.3847/1538-4357/ac4698.
- D. Pomarède, R. B. Tully, R. Graziani, H. M. Courtois, Y. Hoffman, and J. Lezmy. Cosmicflows-3: The South Pole Wall. *apj*, 897(2):133, July 2020. doi: 10.3847/1538-4357/ab9952.
- F. Qin, C. Howlett, L. Staveley-Smith, and T. Hong. Bulk flow and shear in the local Universe: 2MTF and cosmicflows-3. *Monthly Notices of the Royal Astronomical Society*, 482(2):1920–1930, 10 2018. ISSN 0035-8711. doi: 10.1093/mnras/sty2826. URL <https://doi.org/10.1093/mnras/sty2826>.
- S. Raychaudhury. The distribution of galaxies in the direction of the 'Great Attractor'. *nat*, 342(6247):251–255, Nov. 1989. doi: 10.1038/342251a0.
- A. G. Riess, L. M. Macri, S. L. Hoffmann, D. Scolnic, S. Casertano, A. V. Filippenko, B. E. Tucker, M. J. Reid, D. O. Jones, J. M. Silverman, R. Chornock, P. Challis, W. Yuan, P. J. Brown, and R. J. Foley. A 2.4% DETERMINATION OF THE LOCAL VALUE OF THE HUBBLE CONSTANT. *The Astrophysical Journal*, 826(1):56, jul 2016. doi: 10.3847/0004-637x/826/1/56. URL <https://doi.org/10.3847/2F0004-637x/2F826%2F1%2F56>.
- A. G. Riess et al. Observational evidence from supernovae for an accelerating universe and a cosmological constant. *Astron. J.*, 116:1009–1038, 1998. doi: 10.1086/300499.
- V. C. Rubin. Differential rotation of the inner metagalaxy. *aj*, 56:47, Jan. 1951. doi: 10.1086/106628.
- V. C. Rubin, N. Thonnard, J. Ford, W. K., and M. S. Roberts. Motion of the Galaxy and the Local Group determined from the velocity anisotropy of distant Sc I galaxies. II. The analysis for the motion. *aj*, 81:719–737, Sept. 1976. doi: 10.1086/111943.
- R. Scaramella, G. Baiesi-Pillastrini, G. Chincarini, G. Vettolani, and G. Zamorani. A marked concentration of galaxy clusters: is this the origin of large-scale motions? *nat*, 338(6216):562–564, Apr. 1989. doi: 10.1038/338562a0.
- D. Scolnic, D. Brout, A. Carr, A. G. Riess, T. M. Davis, A. Dwomoh, D. O. Jones, N. Ali, P. Charvu, R. Chen, E. R. Peterson, B. Popovic, B. M. Rose, C. M. Wood, P. J. Brown, K. Chambers, D. A. Coulter, K. G. Dettman, G. Dimitriadis, A. V. Filippenko, R. J. Foley, S. W. Jha, C. D. Kilpatrick, R. P. Kirshner, Y.-C. Pan, A. Rest, C. Rojas-Bravo, M. R. Siebert, B. E. Stahl, and W. Zheng. The Pantheon+ Analysis: The Full Data Set and Light-curve Release. *ApJ*, 938(2):113, Oct. 2022. doi: 10.3847/1538-4357/ac8b7a.
- D. M. Scolnic, D. O. Jones, A. Rest, Y. C. Pan, R. Chornock, R. J. Foley, M. E. Huber, R. Kessler, G. Narayan, A. G. Riess, S. Rodney, E. Berger, D. J. Brout, P. J. Challis, M. Drout, D. Finkbeiner, R. Lunnan, R. P. Kirshner, N. E. Sanders, E. Schlafly, S. Smartt, C. W. Stubbs, J. Tonry, W. M. Wood-Vasey, M. Foley, J. Hand, E. Johnson, W. S. Burgett, K. C. Chambers, P. W. Draper, K. W. Hodapp, N. Kaiser, R. P. Kudritzki, E. A. Magnier, N. Metcalfe, F. Bresolin, E. Gall, R. Kotak, M. McCrum, and K. W. Smith. The complete light-curve sample of spectroscopically confirmed SNe ia from pan-STARRS1 and cosmological constraints from the combined pantheon sample. *The Astrophysical Journal*, 859(2):101, may 2018. doi: 10.3847/1538-4357/aab9bb. URL <https://doi.org/10.3847/2F1538-4357/2Faab9bb>.
- M. I. Scrimgeour, T. M. Davis, C. Blake, L. Staveley-Smith, C. Magoulas, C. M. Springob, F. Beutler, M. Colless, A. Johnson, D. H. Jones, J. Koda, J. R. Lucey, Y.-Z. Ma, J. Mould, and G. B. Poole. The 6dF Galaxy Survey: bulk flows on 50-70 h⁻¹ Mpc scales. *mnras*, 455(1):386–401, Jan. 2016. doi: 10.1093/mnras/stv2146.

- L. S. Sparke and I. Gallagher, John S. *Galaxies in the Universe: An Introduction*. Cambridge University Press, 2007.
- R. B. Tully and J. R. Fisher. *Nearby galaxies Atlas*. Cambridge University Press, 1987.
- R. B. Tully, D. Pomarède, R. Graziani, H. M. Courtois, Y. Hoffman, and E. J. Shaya. Cosmicflows-3: Cosmography of the Local Void. *apj*, 880(1):24, July 2019. doi: 10.3847/1538-4357/ab2597.
- R. B. Tully, E. Kourkchi, H. M. Courtois, G. S. Anand, J. P. Blakeslee, D. Brout, T. d. Jaeger, A. Dupuy, D. Guinet, C. Howlett, J. B. Jensen, D. Pomarède, L. Rizzi, D. Rubin, K. Said, D. Scolnic, and B. E. Stahl. Cosmicflows-4. *apj*, 944(1):94, Feb. 2023. doi: 10.3847/1538-4357/ac94d8.
- S. J. Turnbull, M. J. Hudson, H. A. Feldman, M. Hicken, R. P. Kirshner, and R. Watkins. Cosmic flows in the nearby universe from Type Ia supernovae. *mnras*, 420(1):447–454, Feb. 2012. doi: 10.1111/j.1365-2966.2011.20050.x.
- M. Visser. Jerk, snap and the cosmological equation of state. *Classical and Quantum Gravity*, 21(11):2603–2615, June 2004. doi: 10.1088/0264-9381/21/11/006.
- R. Watkins, H. A. Feldman, and M. J. Hudson. Consistently large cosmic flows on scales of $100h^{-1}$ Mpc: a challenge for the standard Λ CDM cosmology. *Monthly Notices of the Royal Astronomical Society*, 392(2):743–756, 12 2008. ISSN 0035-8711. doi: 10.1111/j.1365-2966.2008.14089.x. URL <https://doi.org/10.1111/j.1365-2966.2008.14089.x>.
- R. Watkins, T. Allen, C. J. Bradford, A. Ramon, A. Walker, H. A. Feldman, R. Cionitti, Y. Al-Shorman, E. Kourkchi, and R. B. Tully. Analysing the large-scale bulk flow using cosmicflows4: increasing tension with the standard cosmological model. *mnras*, 524(2):1885–1892, Sept. 2023. doi: 10.1093/mnras/stad1984.
- A. M. Whitford, C. Howlett, and T. M. Davis. Evaluating bulk flow estimators for CosmicFlows-4 measurements. *mnras*, 526(2):3051–3071, Dec. 2023. doi: 10.1093/mnras/stad2764.